Nonlinear dynamics of a passive, coherently driven mesoscopic micromaser

C. Balconi, F. Casagrande, and A. Mondini
Dipartimento di Fisica and INFM, Unità di Milano-Università Via Celoria 16, I-20133 Milano, Italy

W. Lange*
California Institute of Technology 12-33, Pasadena, California 91125
(Received 20 October 1995)

A mesoscopic beam of two-level Rydberg atoms, prepared in the lower state, interacts with a coherently driven cavity mode. The dynamics is described by Maxwell-Bloch equations with atomic propagation. On resonance, the system was predicted to exhibit multistability, upper-branch instabilities, and self-pulsing. In the presence of atomic detuning its dynamical behavior is shown to include in addition period doubling, frequency locking, quasiperiodicity, and chaos, thus providing a remarkable example of nonlinear dynamics of a passive autonomous atomic system with propagation. [S1050-2947(96)03807-3]

PACS number(s): 42.65.Sf, 42.65.Pc, 42.50.Fx

I. INTRODUCTION

Multistability and temporal instabilities, as well as self-pulsing behavior, were recently predicted to occur in the resonant interaction of a beam of two-level Rydberg atoms with a microwave cavity mode and a coherent injected signal [1,2]. Here, we extend our previous analysis by investigating system dynamics at finite atomic detuning.

The physical system considered is similar to the micromaser [3], but differs due to the presence of the injected field and a larger number of atoms N in the cavity, which ranges from a few tens to a few hundreds. As the covered regime is intermediate between the micromaser ($N<1$) and ordinary masers ($N\gg 1$), we call the system a mesoscopic micromaser or *mesomaser*. The atoms are assumed to enter the cavity in the lower state, so that the system acts as a nonlinear absorber.

The mesomaser may be employed to explore a parameter range of particular interest in cavity electrodynamics, in which the atom-field coupling constant and the cavity mode linewidth have the same order of magnitude. In the presence of a strong driving field, the suppression of spontaneous emission [4] and the occurrence of cavity-induced transitions in a bichromatic field [5] have been predicted. On the other hand, for a sufficiently weak driving field, the dynamics is governed by atomic cooperation, leading to nonlinear and collective phenomena. Assuming a saturation photon number well above that of the micromaser, the system dynamics can be described semiclassically by Maxwell-Bloch equations (MBE), propagation effects being taken into account [1,2]. For Rydberg transitions, atomic relaxation may be neglected so that the main contribution to the atomic linewidth is transit broadening due to the finite time of flight through the cavity. This leads to remarkable differences compared with the corresponding optical systems. As in optical bistability, more then one stable state exists. However, for Rydberg atoms the rotation of the Bloch vector is not affected by atomic relaxation, which leads to distinctive phenomena such as *multistability*, i.e., the appearance of more then one hysteresis loop, as well as *instabilities* in the upper-branch of the hysteresis curve, and *self-pulsing oscillations*. These effects, predicted for resonant interaction, are presently under experimental investigation. None of them can occur in ordinary absorptive single-mode bistability in the optical range [6], though for beams of two-level atoms crossing an optical resonator (see, e.g., [7]), Rosenberger and Kim recently predicted the occurrence of multistability and temporal instabilities if the transit time is smaller than the spontaneous lifetime [8,9]. These authors have obtained results similar to our steady state analysis, but with multimode effects at the origin of the instabilities, whereas for Rydberg atoms' instabilities are a single-mode phenomenon.

The subject of this paper is the dynamical behavior of the mesomaser. In particular, we extend our previous analysis to the case of *nonresonant* interaction. Steady-state and nonlinear dynamics have been investigated on the basis of MBE including atomic propagation and detuning effects. The linear stability analysis of the stationary solutions has been performed with atomic detuning taken into account. We find that, for moderate detuning, multistability and upper-branch instabilities similar to the resonant case should occur (see also Refs. [8,9]). In contrast, remarkable differences show up in the nonlinear dynamics of the system. In the detuned case the number of independent system variables is doubled with respect to resonance and correspondingly a much richer variety in the dynamical behavior is predicted. By using the driving field amplitude as a control parameter, we report examples of self-pulsing and precipitation as well as period doubling, frequency locking, quasiperiodicity, and chaos. In particular, chaos is approached when the period-doubling behavior, bifurcated from the (period-one) self-pulsing regime, is perturbed by the onset of another independent frequency. Hence the mesomaser is a remarkable example of a passive atomic system exhibiting temporal instabilities and chaotic behavior. Furthermore, this system displays dynamics beyond the wide class of autonomous systems exhibiting Maxwell-Bloch or Lorentz chaos [10,11]. The atomic propagation through the cavity makes the dynamics intrinsically

*Permanent address: Max-Planck-Institut für Quantenoptik, D-85748 Garching, Germany.

space dependent so that the MBE include partial derivatives as well as integrals in the longitudinal coordinate. The studies closest to this aspect of our investigations are some recent ones by Oraevski and co-workers [12] on maser dynamics (with an inverted medium, no injected signal and no detuning).

The organization of the paper is the following. In Sec. II we introduce the mesomaser model, as described by suitably scaled MBE including atomic propagation and detuning effects. The steady state behavior of the system is discussed in Sec. III. In Sec. IV we present the linear stability analysis of the stationary solutions. On this basis, the nonlinear system dynamics is investigated in Sec. V. A discussion of the results is presented in Sec. VI.

II. THE MODEL

We describe the interaction of a monokinetic beam of two-level Rydberg atoms with a spatially uniform mode of a superconducting microwave cavity driven by a coherent field. The average number N of atoms in the cavity is taken to range from a few tens to a few hundreds, while the saturation photon number is assumed to be large enough for the validity of the semiclassical approximation [1,2]. The dynamics of the system is described by the following dimensionless MBE including propagation:

$$\frac{dx(\overline{t})}{d\overline{t}} = -\overline{k}\left[(1+i\theta)x(\overline{t}) - y - 8C\int_0^1 r^-(\overline{z},\overline{t})d\overline{z}\right], \tag{2.1a}$$

$$\left(\frac{\partial}{\partial \overline{t}} + \frac{\partial}{\partial \overline{z}}\right) r^-(\overline{z},\overline{t}) = x(\overline{t}) r_3(\overline{z},\overline{t}) - i\delta r^-(\overline{z},\overline{t}), \tag{2.1b}$$

$$\left(\frac{\partial}{\partial \overline{t}} + \frac{\partial}{\partial \overline{z}}\right) r_3(\overline{z},\overline{t}) = -\frac{1}{2}[x(\overline{t}) r^+(\overline{z},\overline{t}) + \text{c.c.}], \tag{2.1c}$$

together with the complex conjugates of Eqs. (2.1a,2.1b). Here, $\overline{t}$ and $\overline{z}$ are time and space variables

$$\overline{t} = t/\tau, \quad \overline{z} = z/v\tau \quad (0 \leqslant \overline{z} \leqslant 1), \tag{2.2}$$

scaled to the atomic transit time $\tau = L/v$, L being the cavity length and v the atomic velocity. The Maxwell equation (2.1a) describes the time evolution of the complex dimensionless amplitude of the cavity mode,

$$x = \Omega\tau = 2g\alpha\tau, \tag{2.3}$$

where $|\Omega| = 2g|\alpha|$ is the Rabi frequency, g the Jaynes-Cummings coupling constant, and $|\alpha|^2$ the mean photon number. The evolution of the cavity mode amplitude x results from the interplay of the decay due to the coupling to the environment, the input from the driving field, and the dipole coupling with the atomic polarization distributed along the cavity. These three processes are governed by the parameters

$$\overline{k} = k\tau, \tag{2.4a}$$

$$y = \Omega_{\text{in}}\tau = 2g\alpha_{\text{in}}\tau, \tag{2.4b}$$

$$C = Ng^2\tau^2/4\overline{k}, \tag{2.4c}$$

where k is the linewidth of the cavity mode, y the dimensionless amplitude of the coherent driving field, which is taken to be real, and C the cooperation parameter.

Equations (2.1b,2.1c) are the Bloch equations with atomic propagation for the evolution in space and time of the slowly varying one-atom complex polarization $r^{\pm}$ and population inversion $2r_3$. Note the absence of atomic relaxation terms, which are negligible for Rydberg transitions. The conservation of the modulus of the Bloch vector follows, $r^+r^- + r_3^2 = 1/4$. Another consequence is that the atomic linewidth is set by the inverse time of flight, $1/\tau$. The parameters δ and θ describe the effects of atomic and cavity detuning, respectively:

$$\delta = (\omega_a - \omega_{\text{in}})\tau, \tag{2.5a}$$

$$\theta = (\omega_c - \omega_{\text{in}})\tau/\overline{k}, \tag{2.5b}$$

where ω_a is the (angular) frequency of the transition between the two Rydberg levels, ω_{in} the (reference) frequency of the external signal, and ω_c the cavity mode frequency.

We assume that all atoms enter the cavity (plane $\overline{z} = 0$) in the lower level, so that the boundary conditions for the MBE are

$$r^{\pm}(0,\overline{t}) = 0, \quad r_3(0,\overline{t}) = -1/2. \tag{2.6}$$

Hence the system operates as a *nonlinear absorber*.

III. STEADY-STATE REGIME WITH DETUNING EFFECTS

At steady state, the Bloch equations (2.1b,2.1c) with the boundary conditions (2.6) are easily solved for $r^{\pm}(\overline{z}), r_3(\overline{z})$:

$$r^-(\overline{z}) = -\frac{x}{2X}\left\{\sin(X\overline{z}) - i\delta\frac{1-\cos(X\overline{z})}{X}\right\}, \tag{3.1a}$$

$$r_3(\overline{z}) = -\frac{1}{2} + \frac{|x|^2}{X^2}\sin^2\left(\frac{X\overline{z}}{2}\right) = -\frac{1}{2} + P_{\uparrow}(\overline{z}), \tag{3.1b}$$

where

$$X = \sqrt{|x|^2 + \delta^2} \tag{3.2}$$

is the generalized Rabi frequency and $P_{\uparrow}(\overline{z})$ the occupation probability of the upper level. Its expression at the cavity exit (plane $\overline{z} = 1$)

$$P_{\uparrow}^{\text{out}} = \frac{|x|^2}{X^2}\sin^2\left(\frac{X}{2}\right) \tag{3.3}$$

is particularly important, since all experimental information on system dynamics is obtained by monitoring the populations of the atomic levels outside of the cavity by the field ionization technique [3].

Substitution of (3.1) into the field equation (2.1a) gives the $(x-y)$ state equation [1]:

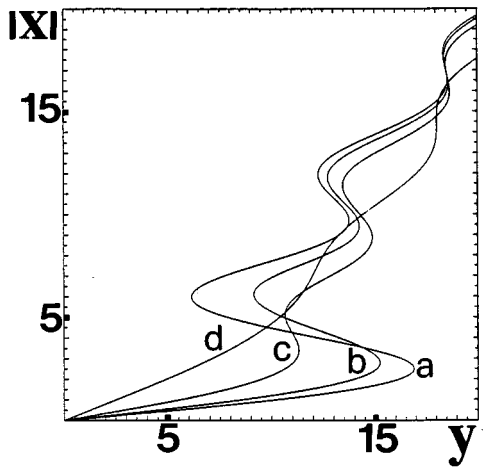

FIG. 1. Steady state with atomic detuning. Cavity field modulus $|x|$ vs driving field amplitude y, from Eq. (3.6) with $C=5, \theta=0$, and atomic detuning (a) $\delta=0$, (b) $\delta=2.5$, (c) $\delta=4.5$, and (d) $\delta=10$.

$$y=x\left[1+4C\frac{1-\cos X}{X^2}+i\left(\theta-4C\delta\frac{1-\mathrm{sinc}X}{X^2}\right)\right], \quad (3.4)$$

where $\mathrm{sinc}X=\sin X/X$. On resonance ($\delta=\theta=0$, $X=x$) Eq. (3.4) reduces to the state equation of absorptive multistability [1]

$$y=x+4C\frac{1-\cos x}{x}. \quad (3.5)$$

Essentially the same expressions were obtained independently by Rosenberger and Kim [8,9], though our model is tailored for the mesomaser, whereas in the optical domain some supplementary assumptions are required (see also Sec. VI). Before investigating the stability of the stationary solutions (3.1) and (3.4), we illustrate briefly the effects of atomic and cavity detuning on steady state behavior. To this end, we rewrite the state equation (3.4) in terms of the modulus of the cavity mode amplitude:

$$y=|x|\left[\left(1+4C\frac{1-\cos X}{X^2}\right)^2+\left(\theta-4C\delta\frac{1-\mathrm{sinc}X}{X^2}\right)^2\right]^{1/2}. \quad (3.6)$$

Let us first set $\theta=0$ (no cavity detuning) to describe the effect of atomic detuning δ. In Fig. 1 we show the behavior of the cavity field modulus $|x|$ as a function of the driving field amplitude y as follows from Eq. (3.6) for a fixed value of the cooperation parameter, $C=5$, and different values of the atomic detuning δ. On resonance, $\delta=0$, we see an example of multistable behavior (tristability). Note the presence of bleaching points, where there is full transmission ($x=y$). These points correspond to stationary states in which the atoms perform an integer number of Rabi nutations during the time of flight through the cavity. Off resonance we see that the presence of an increasing atomic detuning brings about a progressive rectification of the steady state curve, which first becomes bistable and then simply monostable. In the limit $\delta\gg1$, setting $\theta=0$ in Eq. (3.6) gives $|x|\lesssim y$, because both the absorptive and the dispersive oscillating nonlinearities become strongly attenuated.

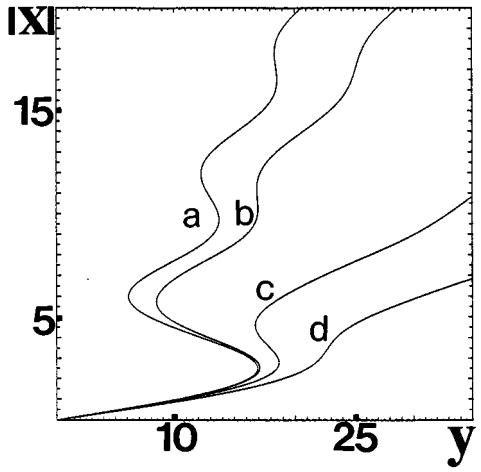

FIG. 2. Steady state with cavity detuning. Cavity field modulus $|x|$ vs driving field amplitude y, from Eq. (3.6) with $C=5, \delta=0$, and cavity detuning (a) $\theta=0$, (b) $\theta=1$, (c) $\theta=3$, and (d) $\theta=5$.

Let us now examine the complementary situation with $\delta=0$ but nonvanishing cavity detuning θ. In Fig. 2 we show the steady state diagram $|x|$ versus y from Eq. (3.6) with $C=5$ as in Fig. 1, but for different values of θ. The effects of frequency mismatch between the cavity mode and the incident field turn out to be rather dramatic. By increasing the parameter θ, we see that not only is the curve rectified progressively, but also the power level of the cavity mode is decreased strongly. Actually, from Eq. (3.6) (with $\delta=0$) we can easily check that, in the limit $\theta\gg1$, the function $|x|(y)$ approaches a linear behavior $|x|\simeq y/\theta$ for $|x|\gg1$, so that eventually $|x|\ll y$.

In the following we shall consider the effect of atomic detuning δ, assuming that the cavity mode is resonantly driven ($\theta=0$). This choice is mainly motivated by the above analysis. Furthermore, we shall see that while the presence of cavity detuning does not increase the complexity of numerical simulations, it would make the linear stability analysis more involved than necessary.

IV. LINEAR STABILITY ANALYSIS WITH ATOMIC DETUNING

As a first step in the linear stability analysis of the stationary solutions of the mesomaser dynamics [Eqs. (3.1) and (3.4)], we introduce a decomposition into real and imaginary parts of the field and polarization variables, setting

$$x(\overline{t})=x_1(\overline{t})+ix_2(\overline{t}), \quad (4.1a)$$

$$r^{\mp}(\overline{z,t})=w_1(\overline{z,t})\pm iw_2(\overline{z,t}), \quad (4.1b)$$

$$r_3(\overline{z,t})=w_3(\overline{z,t}). \quad (4.1c)$$

The MBE (2.1) (with $\theta=0$) become

$$\frac{dx_i(\overline{t})}{dt}=-\overline{k}\left[x_i(\overline{t})-y\delta_{i,1}-8C\int_0^1 w_i(\overline{z,t})d\overline{z}\right] \quad (i=1,2), \quad (4.2a)$$

$$\left(\frac{\partial}{\partial \bar{t}}+\frac{\partial}{\partial \bar{z}}\right) w_{1,2}(\bar{z},\bar{t}) = x_{1,2}(\bar{t}) w_3(\bar{z},\bar{t}) \pm \delta w_{2,1}(\bar{z},\bar{t}), \tag{4.2b}$$

$$\left(\frac{\partial}{\partial \bar{t}}+\frac{\partial}{\partial \bar{z}}\right) w_3(\bar{z},\bar{t}) = -[x_1(\bar{t}) w_1(\bar{z},\bar{t}) + x_2(\bar{t}) w_2(\bar{z},\bar{t})], \tag{4.2c}$$

where $\delta_{i,1}$ is the Kronecker symbol.

Next we consider small fluctuations around the stationary solutions, with an assumed exponential time dependence:

$$x_i(\bar{t}) = x_{is} + [\exp(\bar{\lambda}\bar{t})\,\delta x_i^{(0)} + \text{c.c.}] \quad (i=1,2), \tag{4.3a}$$

$$w_j(\bar{z},\bar{t}) = w_{js}(\bar{z}) + [\exp(\bar{\lambda}\bar{t})\,\delta w_j^{(0)}(\bar{z}) + \text{c.c.}] \quad (j=1,2,3). \tag{4.3b}$$

A stationary state will be stable if and only if $\mathrm{Re}\bar{\lambda}<0$ for each solution $\lambda \equiv \lambda\tau$ of the eigenvalue problem for the linearized dynamics. By inserting expressions (4.3), the linearized version of Eqs. (4.2) reads

$$\bar{\lambda}\delta x_i^{(0)} = -\bar{k}\left(\delta x_i^{(0)} - 8C\int_0^1 \delta w_i^{(0)}(\bar{z})\,d\bar{z}\right) \quad (i=1,2), \tag{4.4a}$$

$$\left(\bar{\lambda}+\frac{\partial}{\partial \bar{z}}\right)\delta w_{1,2}^{(0)}(\bar{z}) = x_{1s,2s}\,\delta w_3^{(0)}(\bar{z}) + w_{3s}(\bar{z})\,\delta x_{1,2}^{(0)} \pm \delta\,\delta w_{2,1}^{(0)}(\bar{z}), \tag{4.4b}$$

$$\left(\bar{\lambda}+\frac{\partial}{\partial \bar{z}}\right)\delta w_3^{(0)}(\bar{z}) = -[x_{1s}\,\delta w_1^{(0)}(\bar{z}) + w_{1s}(\bar{z})\,\delta x_1^{(0)} + x_{2s}\,\delta w_2^{(0)}(\bar{z}) + w_{2s}(\bar{z})\,\delta x_2^{(0)}]. \tag{4.4c}$$

The three linearized Bloch equations (4.4b,4.4c) with the initial conditions $\delta w_j^{(0)}(0)=0$ can be solved for the deviations $\delta w_j^{(0)}(\bar{z})$, providing the expressions of $\delta w_{1,2}^{(0)}(\bar{z})$ to be integrated in the right-hand side (rhs) of the linearized Maxwell equation (4.4a). Note that these latter equations would be coupled in the presence of a finite cavity detuning θ, so that the subsequent calculations would be even lengthier. After carrying out the integrations, we obtain the following linear homogeneous set of eigenvalue equations:

$$(\bar{\lambda}+\bar{k}-\gamma J_1)\,\delta x_1^{(0)} - \gamma J_2\,\delta x_2^{(0)} = 0, \tag{4.5a}$$

$$(\bar{\lambda}+\bar{k}-\gamma J_1')\,\delta x_2^{(0)} - \gamma J_2'\,\delta x_1^{(0)} = 0, \tag{4.5b}$$

where

$$\gamma = \frac{4C\bar{k}}{X^2(\bar{\lambda}^2+X^2)} \tag{4.6}$$

and the expressions for the quantities $J_i, J_i'(i=1,2)$ as functions of $x_{1s}, x_{2s}, \bar{\lambda}, \delta$ are reported in Appendix A.

From Eqs. (4.5) we finally derive the characteristic equation for the eigenvalue $\bar{\lambda}$:

$$(\bar{\lambda}+\bar{k})^2 - \gamma(\bar{\lambda}+\bar{k})(J_1+J_1') + \gamma^2(J_1J_1' - J_2J_2') = 0. \tag{4.7}$$

Instead of solving Eq. (4.7) directly, we consider the parameter space $(C,\bar{k},\delta,y)$ of the system and determine the boundary between the stable and unstable regions of the stationary solutions. One part of the instability boundary is set by the change of sign of a real eigenvalue of the characteristic equation (4.7), i.e., by the condition for the change of stability $\bar{\lambda}=0$. Taking the limit $\bar{\lambda}\to 0$, after some calculations we find that Eq. (4.7) reduces to

$$\frac{y}{X}\frac{dy}{dX} = 0. \tag{4.8}$$

Condition (4.8) is satisfied when $dy/dX=0$, that is the off-resonance generalization of the well-known result, $dy/dx=0$, which proves the instability of all negative-slope branches of the stationary $(x-y)$ diagram, in agreement with elementary physical considerations.

The remaining part of the instability boundary is determined by the change of sign of the real part of two complex conjugate eigenvalues. Hence in Eq. (4.7) we set

$$\bar{\lambda} = i\bar{\nu}, \tag{4.9}$$

where $\bar{\nu} \equiv \nu\tau$ is a dimensionless frequency. When this part of the boundary is crossed, the system undergoes a Hopf bifurcation in which a stationary state (fixed point in phase space) loses its stability, being replaced by a state oscillating at frequency ν (limit cycle). By inserting (4.9) into the characteristic equation (4.7), separating the real and the imaginary parts, and using the expressions of J_i and J_i', after lengthy calculations we obtain the following two equations:

$$\bar{k}^2 - \bar{\nu}^2 - \gamma\{[\bar{k}(a+b) - \bar{\nu}(e+f)]|x_s|^2 + 2\delta^2(d\bar{k}+h\bar{\nu})\} + \gamma^2\{[(ab-ef) - \delta^2(nl+2qr)]|x_s|^4 + \delta^2([d(a+b) + h(e+f) + m(n-l) + p(q+2r)] + \delta^2[n(n-l) - 2r(q+2r)])|x_s|^2 + \delta^2[(m^2-p^2) + \delta^2((d^2-h^2) + 2(mn+2pr)) + \delta^4(n^2-4r^2)]\} = 0, \tag{4.10a}$$

$$2\bar{k}\bar{\nu} - \gamma\{[\bar{\nu}(a+b) + \bar{k}(e+f)]|x_s|^2 + 2\delta^2(d\bar{\nu}-h\bar{k})\} + \gamma^2\{[(af+be) + \delta^2(nq-2rl)]|x_s|^4 + \delta^2([-h(a+b) + d(e+f) - p(n-l) + m(q+2r)] + \delta^2[n(q+2r) + 2r(n-l)])|x_s|^2 - 2\delta^2(mp - \delta^2[2mr - np - dh] - 2\delta^4 nr)\} = 0, \tag{4.10b}$$

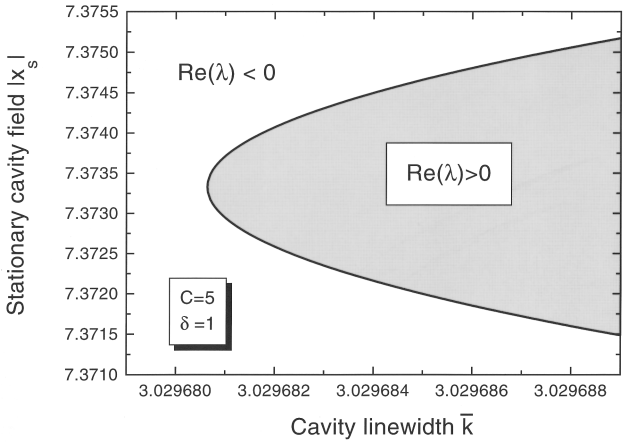

FIG. 3. Boundary in the $|x|_s$-$\bar{k}$ plane of parameter space for nontrivial instability in the first upper branch, obtained from the two solutions $|x_s|_1$ and $|x_s|_2$ to Eqs. (4.10). The steady state is unstable in the shaded region. Fixed parameters are $C=5$, $\delta=1$.

where the expressions for the quantities $a,b,\ldots,r$ are reported in Appendix B. Instead of the parameter y, corresponding to the incident field amplitude, we use the stationary value of the cavity field modulus $|x_s|$, which is linked to y by the state equation (3.6). This is possible as all field strengths can be expressed in terms of $|x_s|$.

We have studied Eqs. (4.10) numerically. For a set of fixed values for the parameters (C,k,δ) there is either no real solution, if the system is stable, or there are two solutions for the quantities $(|x_s|_i,\bar{\nu}_i)_{(i=1,2)}$. In the latter case the system displays oscillatory behavior ($\mathrm{Re}\lambda>0$) for stationary cavity field values in the region bounded by the two solutions $|x_s|_1$ and $|x_s|_2$. This boundary between stable and unstable steady states in the $|x_s|$-k plane of parameter space is shown in Fig. 3 for fixed C and δ. Crossing the boundary at a bifurcation point $|x_s|_i$, the system starts oscillating spontaneously with a small amplitude at frequency $\nu=\bar{\nu}_i/\tau$. Thus, the numerical solution of Eqs (4.10) allows us to determine the regions of instability of the system, as well as the oscillation frequency at the instability boundary.

From Fig. 3 it is evident that oscillatory behavior can only occur if k exceeds a threshold value, defined by the vertex of the parabolic instability boundary. In Fig. 4 we show this threshold value of k as a function of the remaining two phase-space parameters C and δ. Generally, for nontrivial temporal instabilities to occur the cooperation parameter C must be large enough for multistability and the product Ck, which controls the atom-field coupling [see the rhs of Eq. (2.1a)], must satisfy the inequality $Ck\gg 1$. By the definitions (2.4), this inequality implies that $g\sqrt{N}>1/\tau$, which means that the atoms can cooperatively interact with the cavity field at a rate larger than transit broadening. With increasing δ, the values of k and C at which self-pulsing sets in increase, as demonstrated in Fig. 4.

As a relevant example, in Fig. 5 we show the results for the stability of the stationary states when the system is multistable and detuned ($C=5$ and $\delta=0.4$) for different values of the loss parameter k. Instabilities on positive-slope upper branches of the $(|x|-y)$ state diagram appear at $k\simeq 1.4$; their extension grows with increasing values of k, while small

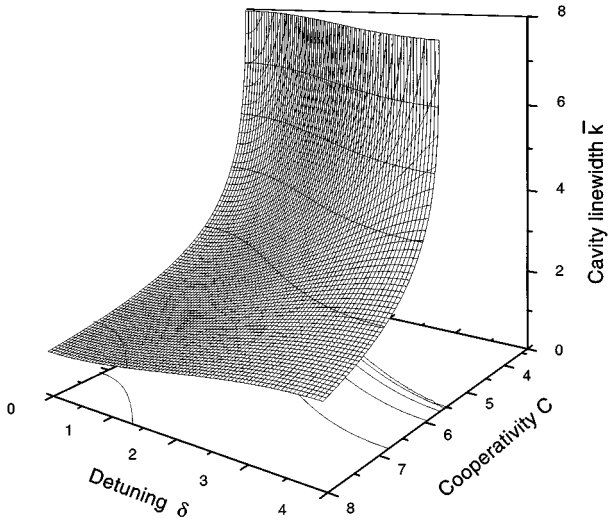

FIG. 4. Threshold for the occurrence of instability in the first upper branch of the steady-state solution, displayed as a surface in the space spanned by the parameters C,δ, and $\bar{k}$. The system displays spontaneous oscillations for points above the plotted surface. Note the divergence for small values of C, corresponding to stable behavior even for arbitrarily large values of k.

unstable intervals appear also in the upper part of the lower positive-slope branch. Eventually, as for $k=5.7$ in Fig. 5 the system exhibits an instability continuum from the lower to the upper positive-slope branches, through the (trivially unstable) negative-slope branch. From these results it follows that the presence of moderate detuning, $\delta\lesssim 1$, does not substantially modify the instability conditions as well as their physical interpretation encountered in the resonant situation [2]. Dramatic differences from the resonant case, however, show up in the mesomaser dynamics.

V. NONLINEAR DYNAMICS

To describe the dynamics of the system we numerically integrated the MBE (2.1) with atomic propagation and detuning effects, adapting a method devised by Risken and

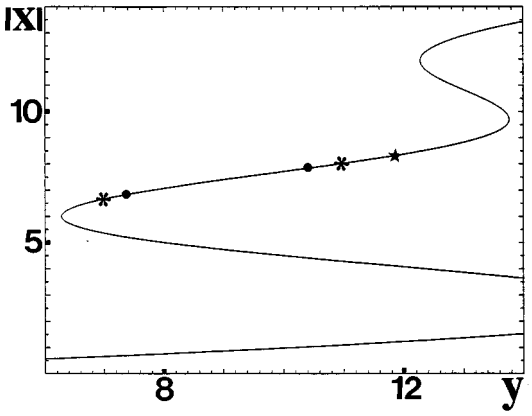

FIG. 5. Upper-branch instability boundaries in the $(|x|-y)$ diagram, from Eqs. (4.10) with $C=5,\delta=0.4$, and $\bar{k}=3$ (●), $k=3.5$ (*), $\bar{k}=5.7$ (⋆).

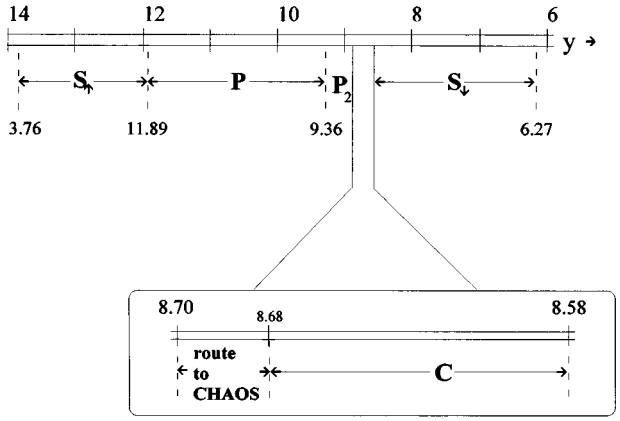

FIG. 6. Dynamical regimes for decreasing values of the driving field amplitude y, starting from the upper branch of the $(|x|-y)$ curve for $C=5, \delta=0.4, k=5.7$. $S_{\uparrow}$ ($S_{\downarrow}$) denotes the stationary state on the upper (lower) branch; P denotes periodic (self-pulsing) regime; $P2$ denotes the period-doubling regime. In the inset, C is the chaotic regime; see text for the route to chaos.

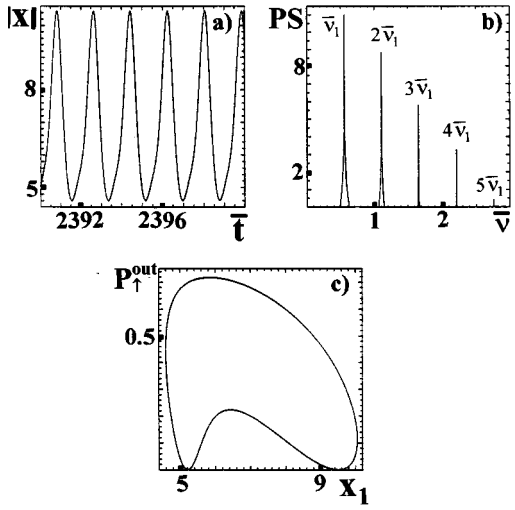

FIG. 7. Self-pulsing regime. (a) Long-time behavior of the cavity field modulus $|x|$. (b) Power spectrum (PS) of cavity field (logarithmic power scale). (c) Limit cycle in the $(x_1, P_{\uparrow}^{\text{out}})$ projection of phase space. From Eqs. (C2) with $C=5$, $k=5.7$, $\delta=0.4$, $y=9.3659$.

Nummedal [13]. Some details are given in Appendix C. Our goal was to obtain the time evolution of the system variables at the exit of the cavity, which corresponds to the only experimentally accessible information. From the number of independent variables and parameters, which is four in both cases, we expected the possibility to observe interesting dynamical behavior. On the other hand, we were guided by the previous analysis of the system's steady state together with the results on resonant dynamics reported in Ref. [2]. Therefore, we present results for parameter ranges considered in the previous sections, obtained by using the incident field amplitude y as the control parameter. More precisely, we fixed the parameters C, k, δ at values ($C=5$, $k=5.7$, $\delta=0.4$) for which we know that the system is multistable and presents nontrivial temporal instabilities on upper branches of the $(|x|-y)$ steady-state curve (see Fig. 5). Then we integrated the MBE (2.1) with boundary conditions (2.6) for different values of y, choosing initial values of the cavity mode variables very close to stationary points of the $(|x|-y)$ diagram.

The results of the numerical simulations are summarized in Fig. 6, where the different dynamical regimes are indicated for decreasing values of the control parameter y. For $y \geqslant 11.897$ the linear analysis of Sec. IV predicts the stability of upper-branch stationary states. Accordingly, we find that after a short transient the system approaches the predicted steady state ($S_{\uparrow}$ in Fig. 6). The trajectories approach a fixed point, which is the simplest attractor in the phase space associated with the system. As y reaches the predicted instability boundary for the Hopf bifurcation, $y=11.896$, the system spontaneously develops undamped oscillations (self-pulsing behavior), i.e., a periodic regime (P in Fig. 6) described by a limit cycle in phase space. At this instability threshold the value of the frequency of self-pulsing oscillations turns out to be in excellent agreement with the prediction of the linear stability analysis. This value, $\overline{\nu_1}=\nu_1\tau=0.72$, is within the atomic linewidth $1/\tau$ set by the inverse transit time, as expected for a single-mode instability. If one displaces the system from steady state in the stable region just above the Hopf bifurcation (i.e., with y slightly above the bifurcation value), the cavity mode amplitude relaxes to steady state through damped oscillations, whose broad power spectrum has a maximum just at $\overline{\nu}=\overline{\nu_1}$. As the bifurcation is crossed, the power spectrum undergoes a spectacular narrowing to a line at $\overline{\nu}=\overline{\nu_1}$. An example of self-pulsing behavior is illustrated in Fig. 7. We shall see that the oscillation at ν_1 will survive through all dynamical regimes, with its value slowly decreasing towards $1/2\tau$ as y decreases. The power spectrum of system variables displays the presence of harmonics of the self-pulsing frequency $\overline{\nu_1}$, whose weight grows as the periodic oscillations become more and more irregular.

The amplitude of self-pulsing oscillations, which is small close to the bifurcation, initially increases as the control parameter y decreases. Let us recall that on resonance [2] the oscillation amplitude eventually either (for smaller values of k) decreases approaching the other bifurcation point, or (for higher values of k) is suddenly interrupted by the occurrence of a precipitation on the lower positive-slope branch, where another stationary state is available. Hence, self-pulsing and precipitation exhaust the dynamical effects occurring on resonance. This is not the case in the presence of atomic detuning.

The self-pulsing regime lasts until the control parameter reaches a value $y=9.359$, where a subharmonic bifurcation or period doubling occurs (P2 in Fig. 6). An example of period doubling behavior is illustrated in Fig. 8. The power spectrum shows the characteristic structure with all harmonics of the frequency $\overline{\nu_1}/2$, while the line at $\overline{\nu}=\overline{\nu_1}$ remains the dominant one. As y is further decreased, these period-doubled oscillations persist down to $y=8.70$. Only in the final portion of this interval, for some values of y between 8.79 and 8.74, another frequency $\overline{\nu_2}<\overline{\nu_1}$ appears in the power spectrum. However, this new frequency is commensurate with the old ones, the ratio being a rational number

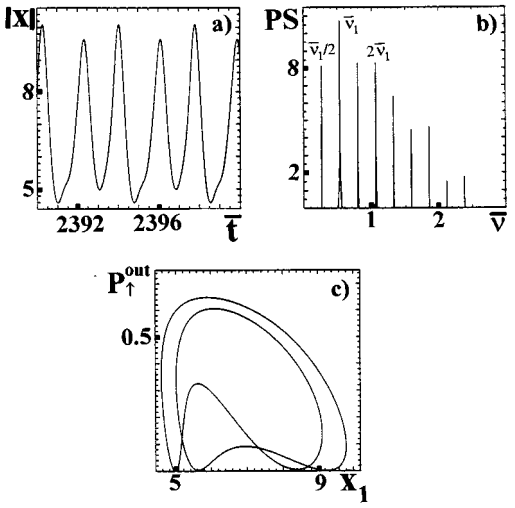

FIG. 8. Period-doubling regime. Same plots as in Fig. 5 for $y=8.9322$.

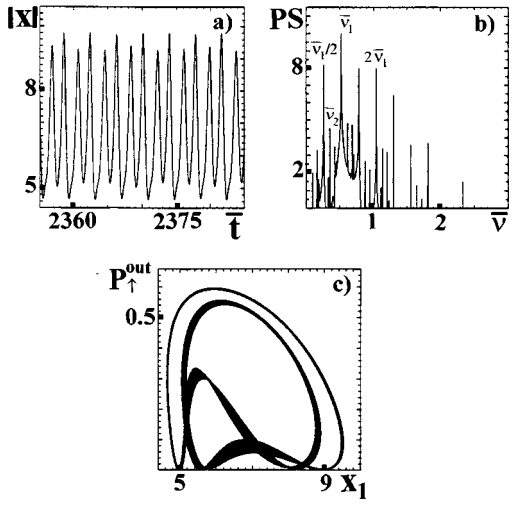

FIG. 10. Route to chaos. Same plots as in Figs. 5–7, for $y=8.6844$. The power spectrum (b) shows the coexistence of period doubling and quasiperiodicity due to the presence of a new and incommensurate frequency (see text).

$(\overline{\nu_1}/\overline{\nu_2}=3/2)$. More precisely, $\overline{\nu_2}$ appears to be locked with $\overline{\nu_1}/2$, in such a way that the power spectrum shows a series of lines at all multiples of a basic frequency $\overline{\nu_1}/6=(\overline{\nu_1}/2)/3=\overline{\nu_2}/4$, as shown in Fig. 9.

At $y=8.70$, while the system still exhibits period-doubling behavior, a frequency $\overline{\nu_2}$ appears in the power spectrum, but this time frequency locking does not occur $(\overline{\nu_1}/\overline{\nu_2}<3/2)$, so that quasiperiodicity is introduced in the dynamics. As shown in Fig. 10, besides the dominant lines at harmonics of $\overline{\nu_1}/2$ (period-doubling structure), the power spectrum displays an emerging substructure with $\overline{\nu_2}$ and the combination tones between $\overline{\nu_1}/2$ and $\overline{\nu_2}$ (quasiperiodic structure). This process builds up rapidly (see Fig. 10 for $y=8.6844$), until suddenly, as y is decreased very slightly (see Fig. 11 for $y=8.6843$), the system apparently enters a chaotic regime (C in Fig. 6), corresponding to the motion on a strange attractor in phase space. The time evolution of the system variables as well as the trajectories in phase space become unpredictable. The main indication of the occurrence of deterministic chaos comes from the power spectrum, which suddenly broadens to a continuum of frequencies while its profile becomes very noisy. The only clear trace of all past dynamical regimes survives in some sharp lines at $\overline{\nu_1}$ and a few of its harmonics and (occasionally) subharmonics, where the values of $\overline{\nu_1}$ are close to 0.5, i.e., $\nu_1 \geqslant 1/2\tau$. The route of the system to chaos appears to be via the onset of an incommensurate frequency $\overline{\nu_2}$, which destabilizes the period-doubling regime described by the frequencies $\overline{\nu_1}$ and $\overline{\nu_1}/2$. The problem of better characterizing and proving the existence of a chaotic regime will be addressed in Sec. VI.

The chaotic behavior is observed in the range

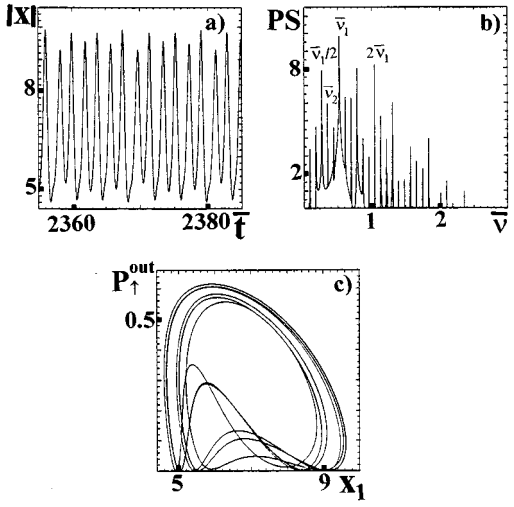

FIG. 9. Frequency locking regime. Same plots as in Figs. 5 and 6 for $y=8.7617$. Note the period-six oscillations, due to the presence of a new and commensurate frequency (see text).

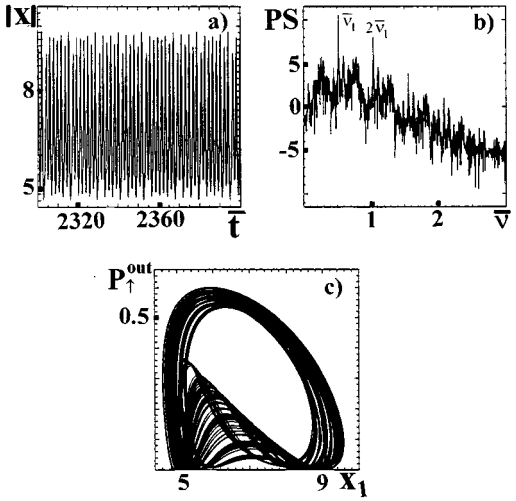

FIG. 11. Chaos. Same plots as in Figs. 5–8, for $y=8.6843$. Note the dramatic change in the power spectrum (b) with respect to the previous one [8(b)].

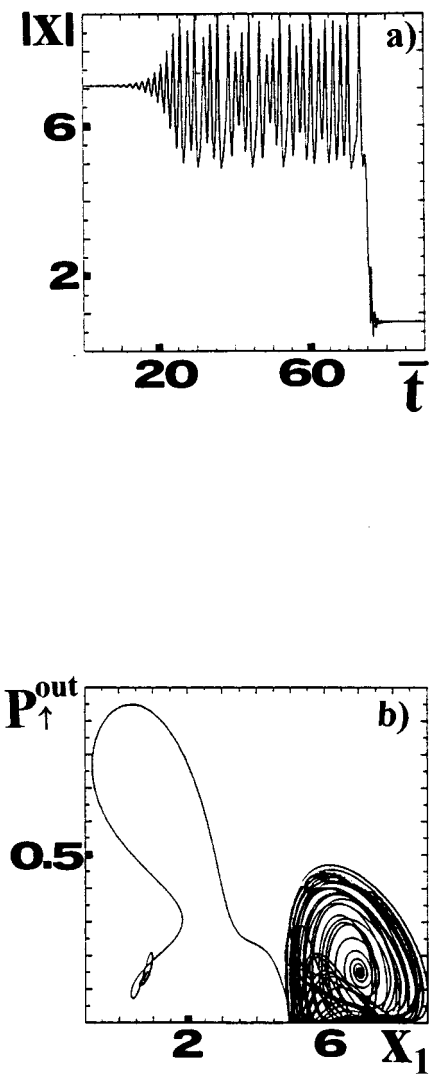

FIG. 12. Precipitation from upper to lower positive-slope branch of the $(|x|-y)$ diagram. (a) Time evolution of cavity field modulus $|x|$. (b) Trajectory of the representative point in the $(x_1, P_{\uparrow}^{out})$ projection of phase space. Same parameters as in Figs. 5–9, except $y=8.0063$.

$8.68 \geqslant y \geqslant 8.58$. For lower values of y (see Fig. 12), the strong irregular oscillations make the system escape from the basin of attraction of the strange attractor, and approach a simple fixed point. In relation to the $(|x|-y)$ state diagram, we can say that the time evolution of the system ends with the precipitation from unstable stationary states on the positive-slope upper branch, down to stable states on the positive-slope lower branch ($S_{\downarrow}$ in Fig. 6).

VI. CONCLUSIONS

We have investigated the dynamics of a passive, coherently driven, mesoscopic micromaser or *mesomaser*. Generalizing our previous treatment [1,2] we have included atomic detuning in the MBE with atomic propagation, describing the system dynamics in the semiclassical approximation. In these equations atomic relaxation is neglected, which is reasonable for a beam of Rydberg atoms. As a consequence, the modulus of the atomic Bloch vector is conserved, the atomic linewidth is determined by transit broadening, and dissipation enters the nonlinear system only via the cavity decay.

The steady-state analysis shows the occurrence of multistability and nontrivial temporal instabilities (Hopf bifurcations) on upper branches of the state diagram of cavity field versus incident field amplitude. Starting from these results, and by using the external coherent field amplitude as a control parameter, we have investigated the time evolution of the system variables at the cavity exit, which are the experimentally relevant quantities.

Sampling the system with decreasing values of y, we first found the onset of spontaneous undamped oscillations (self-pulsing) occurring at the instability threshold, the oscillation frequency corresponding to that predicted by the stability analysis. This frequency is equal to the control frequency of relaxation oscillations observed when the system is displaced from a stable stationary state. Self-pulsing originates from a cooperative behavior of the mesoscopic atomic system, which leads to an oscillatory energy exchange between atoms and cavity field occurring at a rate larger that the inverse atomic transit time $1/\tau$. In this case the system can self-organize and develop periodic oscillations at frequencies that are smaller than, or comparable, to $1/\tau$. In particular, for decreasing values of y, the self-pulsing frequency ν_1 decreases slowly, approaching the value $1/2\tau$.

In contrast to the resonant case, where only self-pulsing and (for proper values of k) precipitation to a lower stable state can take place, the self-pulsing behavior leads to a subharmonic bifurcation (period doubling). Near the end of the period-doubling regime, another oscillation frequency, $\nu_2 < \nu_1$, is generated for some values of y, but is always locked to the first frequency, so that the dynamics remains periodic. At the very end of the period-doubling regime, a frequency ν_2 is generated again, but this time it is incommensurate to ν_1. Thus period doubling, which gives the dominating periodic structure of the power spectrum of system variables, coexists with quasiperiodicity, which gives a substructure of lines at the combination tones of $\nu_1/2$ and ν_2. This situation leads to a very sharp transition to a chaotic regime, observed via a dramatic change in the power spectrum, which develops a broad frequency continuum with a very noisy profile. Eventually the irregular oscillations make the system precipitate to the stationary state available on the low power branch of the stationary diagram.

Several remarks are in order concerning our results. The mesomaser has been shown to be an interesting example of a passive atomic system exhibiting nonlinear oscillations and deterministic chaos. It is also quite different from most dynamical systems exhibiting Maxwell-Bloch or Lorentz chaos. First of all, while the system is autonomous, the atomic variables depend on both time and space. This has consequences for the investigation of chaos. The question of the occurrence of deterministic chaos should be answered by the evaluation of (at least) the maximal Lyapunov exponent, which is positive if nearby orbits in phase space diverge exponentially. This extreme sensitivity of the system to initial conditions is a signature of chaotic dynamics. The point is that the related algorithms have been developed for ordinary autonomous systems. We are presently working on a generalization that may be suitable to our system whose dy-

namics depend on both time and space variables.

Another remarkable difference with systems described semiclassically by MBE is the absence of atomic relaxation, which is well justified for Rydberg atoms in the microwave regime. Multistability and instabilities were predicted even in optical domain [8,9] for beams of two-level atoms crossing a resonator. In that regime, however, spontaneous emission may only be neglected for extremely fast atomic beams, and the uniform field limit must be assumed, whereas in the mesomaser suitable conditions exist automatically. An interesting connection with the optical domain is provided by the recently demonstrated *microlaser* [14], which is the optical analog of the micromaser, because in that system the atomic linewidth is really dominated by transit time. Having in mind the passage from the micromaser to the mesomaser, we plan to investigate the concept of a coherently driven *mesolaser*, which could be configurated as a microlaser operating with higher atomic fluxes and with a lower finesse, in order to favor collective atomic behavior in an intermediate-coupling regime.

As for the feasibility of an experimental observation of the effects described in this paper, the main difficulties remain those discussed in the analysis of the resonant case [1,2]. Problems are effects of the atomic velocity distribution, also investigated by Rosenberger and Kim in the optical case [9] and by Oraevski and co-workers for maser amplifiers [12], and inhomogeneous broadening induced by stray fields. Since multistability appears to be experimentally accessible, and actually is under experimental investigation, we are confident that dynamical effects may be observed in the laboratory as well.

ACKNOWLEDGMENTS

We thank Professor. A. Giorgilli and Professor L.A. Lugiato for their interest in this work and some stimulating (sometimes chaotic) discussions.

APPENDIX A

In this appendix we report expressions for the quantities J_i, J_i' $(i=1,2)$ which appear in the eigenvalues equations (4.5) and the characteristic equation (4.7) of the linear stability analysis of the system:

$$J_1(x_{1s},x_{2s},\overline{\lambda},\delta)=\frac{x_{2s}}{\overline{\lambda}}(\delta x_{1s}+\overline{\lambda}x_{2s})[(\cos X-e^{-\overline{\lambda}})-\overline{\lambda}\,\mathrm{sinc}X]+\left[x_{1s}^2-\delta(x_{1s}x_{2s}-\overline{\lambda}\delta)\frac{\overline{\lambda^2}-X^2}{\overline{\lambda}(\overline{\lambda^2}+X^2)}\right](1-e^{-\overline{\lambda}}\cos X)$$
$$-\frac{x_{1s}^2}{\overline{\lambda}}\left(1+\frac{\overline{\lambda^2}}{X^2}-e^{-\overline{\lambda}}\right)X\sin X+\delta(x_{1s}x_{2s}-\overline{\lambda}\delta)\left(1-2\frac{x}{\lambda^2+X^2}e^{-\overline{\lambda}}\sin X\right), \tag{A1}$$

$$J_2(x_{1s},x_{2s},\overline{\lambda},\delta)=\frac{x_{2s}}{\overline{\lambda}}(\overline{\lambda}x_{1s}-\delta x_{2s})[\overline{\lambda}\,\mathrm{sinc}X-(\cos X-e^{-\overline{\lambda}})]+\frac{1}{\overline{\lambda}}\left[x_{2s}(\overline{\lambda}x_{1s}+\delta x_{2s})+2\overline{\lambda^2}\delta\frac{x_{1s}^2+\delta^2}{\overline{\lambda^2}+X^2}\right](1-e^{-\overline{\lambda}}\cos X)$$
$$-\frac{x_{1s}x_{2s}}{\overline{\lambda}}\left(1+\frac{\overline{\lambda^2}}{X^2}-e^{-\overline{\lambda}}\right)X\sin X+\delta Xe^{-\overline{\lambda}}\sin X-\delta(x_{1s}^2+\delta^2)\left(1-2\frac{X}{\overline{\lambda^2}+X^2}e^{-\overline{\lambda}}\sin X\right), \tag{A2}$$

$$J_i'(x_{1s},x_{2s},\overline{\lambda},\delta)=J_i(x_{2s},x_{1s},\overline{\lambda},-\delta)\quad(i=1,2). \tag{A3}$$

APPENDIX B

The coefficients $a,b,\ldots,r$ in Eqs. (4.10) are defined as follows:

$$a=1-\cos\overline{\nu}\cos X-X^2\mathrm{sinc}\overline{\nu}\,\mathrm{sinc}X, \tag{B1}$$

$$b=\cos X-\cos\overline{\nu}, \tag{B2}$$

$$d=\frac{1}{X^2-\overline{\nu^2}}[2X^2\overline{\nu^2}\,\mathrm{sinc}\overline{\nu}\,\mathrm{sinc}X-(X^2+\overline{\nu^2})(1-\cos X\cos\overline{\nu})], \tag{B3}$$

$$e=\overline{\nu}\left[\mathrm{sinc}\overline{\nu}\cos X+\mathrm{sinc}X\left(\frac{1-\cos\overline{\nu}}{\overline{\nu^2}}X^2-1\right)\right], \tag{B4}$$

$$f=\overline{\nu}(\mathrm{sinc}\overline{\nu}-\mathrm{sinc}X), \tag{B5}$$

$$h=\overline{\nu}\left[1+\frac{(X^2+\overline{\nu^2})\mathrm{sinc}\overline{\nu}\cos X-2X^2\cos\overline{\nu}\,\mathrm{sinc}X}{X^2-\overline{\nu^2}}\right], \tag{B6}$$

$$l=\mathrm{sinc}\overline{\nu}(1+\cos X)-\mathrm{sinc}X, \tag{B7}$$

$$m=X^2\cos\overline{\nu}\,\mathrm{sinc}X, \tag{B8}$$

$$n=1-2\frac{X^2\cos\overline{\nu}\,\mathrm{sinc}X-\overline{\nu^2}\,\mathrm{sinc}\overline{\nu}\cos X}{X^2-\overline{\nu^2}}, \tag{B9}$$

$$p=X^2\overline{\nu}\,\mathrm{sinc}\overline{\nu}\,\mathrm{sinc}X, \tag{B10}$$

$$q=\frac{1}{\overline{\nu}}(1-\cos\overline{\nu})(1+\cos X), \tag{B11}$$

$$r=\frac{p-\overline{\nu}(1-\cos\overline{\nu}\cos X)}{X^2-\overline{\nu^2}}. \tag{B12}$$

APPENDIX C

In order to integrate numerically the MBE (2.1) with atomic propagation and detuning effects, it is convenient to introduce real and imaginary parts of the field and polarization variables, setting

$$x=x_1+ix_2, \tag{C1a}$$

$$r^{\mp}=\frac{u\pm iv}{2}, \tag{C1b}$$

$$r_3=\frac{w}{2}. \tag{C1c}$$

The MBE (2.1) are transformed into the following set of coupled partial-derivative, integro-differential equations:

$$\frac{dx_1(\overline{t})}{d\overline{t}}=-\overline{k}\left[x_1(\overline{t})-y-4C\int_0^1 u(\overline{z,t})d\overline{z}\right], \tag{C2a}$$

$$\frac{dx_2(\overline{t})}{d\overline{t}}=-\overline{k}\left[x_2(\overline{t})-4C\int_0^1 v(\overline{z,t})d\overline{z}\right], \tag{C2b}$$

$$\left(\frac{\partial}{\partial\overline{t}}+\frac{\partial}{\partial\overline{z}}\right)u(\overline{z,t})=x_1(\overline{t})w(\overline{z,t})+\delta v(\overline{z,t}), \tag{C2c}$$

$$\left(\frac{\partial}{\partial\overline{t}}+\frac{\partial}{\partial\overline{z}}\right)v(\overline{z,t})=x_2(\overline{t})w(\overline{z,t})-\delta u(\overline{z,t}), \tag{C2d}$$

$$\left(\frac{\partial}{\partial\overline{t}}+\frac{\partial}{\partial\overline{z}}\right)w(\overline{z,t})=-x_1(\overline{t})u(\overline{z,t})-x_2(\overline{t})v(\overline{z,t}). \tag{C2e}$$

The boundary conditions (2.6) become

$$u(0,\overline{t})=v(0,\overline{t})=0, \quad w(0,\overline{t})=-1. \tag{C3}$$

By the definitions (C1), the modulus of the atomic Bloch vector, which is constant in the absence of atomic relaxation, is now unitary:

$$u^2+v^2+w^2=1. \tag{C4}$$

In fact, the space and time evolution of the Bloch vector can be described by two angles on the unitary Bloch sphere (polar and azimuthal), thereby reducing the number of equations from five to four, which is of course the number of independent system variables. However, the presence of angles turns out to complicate the numerical integration of the MBE. So we preferred to integrate the set of Eqs. (C2), for which the relation (C4) provides a check at each numerical step.

To integrate the MBE (C2) numerically, we have adapted a method originally developed by Risken and Nummedal for the analysis of laser dynamics [13]. It uses a finite-difference scheme, which is second-order accurate in both space and time. The steps of the scaled time and space grids are taken equal to guarantee the stability of the solution.

[1] F. Casagrande, L.A. Lugiato, W. Lange, and H. Walther, Phys. Rev. A **48**, 790 (1993).

[2] C. Balconi, F. Casagrande, LA. Lugiato, W. Lange, and H. Walther, Opt. Commun. **114**, 425 (1995).

[3] D. Meschede, H. Walther, and G. Müller, Phys. Rev. Lett. **54**, 551 (1985).

[4] W. Lange, and H. Walther, Phys. Rev. A **48**, 4551 (1993).

[5] G.S. Agarwal, W. Lange, and H. Walther, Phys. Rev. A **48**, 4555 (1993); M. Elk and P. Lambropoulos, *ibid.* **50**, 1490 (1994); W. Lange, H. Walther, and G.S. Agarwal, *ibid.* **50**, 3593 (1994).

[6] L.A. Lugiato, in *Progress in Optics*, edited by E. Wolf (North-Holland, Amsterdam, 1984), Vol. XXI, p. 69ff.

[7] G. Rempe, R.J. Thompson, R.J. Brecha, W.D. Lee, and H.J. Kimble, Phys. Rev. Lett. **67**, 1727 (1991); A.T. Rosenberger, L.A. Orozco, H.J Kimble, and P.D. Drummond, Phys. Rev. A **43**, 6284 (1991).

[8] A.T. Rosenberger and Jeong-Mee Kim, Opt. Commun. **101**, 403 (1993).

[9] Jeong-Mee Kim and A.T. Rosenberger, Opt. Commun. **115**, 401 (1995).

[10] See, e.g., J. Opt. Soc. Am. B **2** (1) (1995), special issue on instabilities in active optical media, edited by N.B. Abraham, L.A. Lugiato, and L.M. Narducci; J. Opt. Soc. Am. B **5** (5) (1988), special issue on nonlinear dynamics of lasers, edited by D. K. Brandy, A. N. Oraevski, and J. R. Tredicce.

[11] For a physicist-oriented approach to deterministic chaos, see e.g., P. Bergé, Y. Pomeau, C. Vidal, *L'Ordre dans le Chaos* (Hermann, Paris, 1984).

[12] A.N. Oraevski, T.V. Sarkisyan, D.J. Jones, and D.K. Bandy, Kavantovaya Elekron. (Moscow) **19**, 234 (1992) [Sov. J. Quantum Electron. **22**, 213 (1992)]; D.K. Bandy, J.D. Graham, D.J. Jones, A.N. Oraevski, and T. Sarkisyan, Phys. Rev. A **50**, 685 (1994).

[13] H. Risken and K. Nummedal, J. Appl. Phys. **39**, 4662 (1968).

[14] K. An, J.J. Childs, R.R. Dasari, and M.S. Feld, Phys. Rev. A **73**, 3375 (1994).